Petroleum Science 21 (2024) 1928–1943

Contents lists available at ScienceDirect

Petroleum Science

journal homepage: www.keaipublishing.com/en/journals/petroleum-science

Original Paper

Eco-friendly calcium alginate microspheres enable enhanced profile control and oil displacement

Xiao-Han Zhang [a, b], Chang-Jing Zhou [c], Yuan-Xiang Xiao [c], Bo Hui [c], Yong-Gang Xie [c], Yu-Bin Su [c], Xin-Ru Li [b], Jie Huang [a, b], Mao-Chang Liu [a, b, d, *]

[a] International Research Center for Renewable Energy, State Key Laboratory of Multiphase Flow in Power Engineering, Xi'an Jiaotong University, Xi'an, 710049, Shaanxi, PR China
[b] Shaanxi Key Laboratory of Advanced Stimulation Technology for Oil & Gas Reservoirs, School of Petroleum Engineering, Xi'an Shiyou University, Xi'an, 710065, Shaanxi, PR China
[c] Oil & Gas Technology Research Institute, Changqing Oilfield Branch Company, PetroChina, Xi'an, 710021, Shaanxi, PR China
[d] Suzhou Academy of Xi'an Jiaotong University, Suzhou, 215123, Jiangsu, PR China

ARTICLE INFO

Article history:
Received 29 May 2023
Received in revised form
1 December 2023
Accepted 14 December 2023
Available online 22 December 2023

Edited by Yan-Hua Sun

Keywords:
Calcium alginate microspheres
Wettability
Interfacial tension
Rheology
Viscoelasticity
Enhanced oil recovery (EOR)

ABSTRACT

Polymer microspheres (PMs), such as polyacrylamide, have been widely applied for enhanced oil recovery (EOR), yet with environmental concerns. Here, we report a microfluid displacement technology containing a bio-based eco-friendly material, i.e., calcium alginate (CaAlg) microspheres for EOR. Two dominant mechanisms responsible for EOR over CaAlg fluid have been verified, including the microscopic oil displacement efficacy augmented by regulating capillary force (determined by the joint action of interfacial tension and wettability between different phases) and macroscopic sweep volume increment through profile control and mobility ratio reduction. This comprehensive effectiveness can be further impacted when the CaAlg microsphere is embellished ulteriorly by using appropriate amount of sodium dodecyl sulfonate (SDS). The core flooding and nuclear magnetic resonance (NMR) tests demonstrate that CaAlg-SDS microsphere can balance the interphase property regulation (wettability alteration and IFT reduction) and rheology properties, enabling simultaneous profile control and oil displacement. Excessive introduction of SDS will have a negative impact on rheological properties, which is not favored for EOR. Our results show that the involvement of 4-mM SDS will provide the best behavior, with an EOR rate of 34.38%. This cost-effective and environmentally-friendly bio-microsphere-based microfluidic displacement technology is expected to achieve "green" oil recovery in future oilfield exploitation.

1. Introduction

Petroleum remains a key pillar of the world's energy needs. Unconventional reservoirs have low permeability and high water-cut but are an increasing proportion of existing reserves, and residual oil can remain trapped in these reservoirs (Boul and Ajayan, 2020; Hu et al., 2018). Thus, research is urgently needed to improve oil recovery efficiency and reduce water productivity. In the tertiary oil recovery stage, chemical flooding is used extensively as an effective technology for EOR (Gbadamosi et al., 2018). However, traditional chemical EOR technologies such as surfactant flooding or alkaline flooding are challenged by expensive chemicals, high consumption, chemical loss, and possible reservoir damage (Muggeridge et al., 2014). Recently, research on the application of polymer microspheres/particles (PMs) in oil exploration has been frequently reported. PMs are an effective chemical EOR agent for deep profile control and flooding because PMs can plug the water channel of the high-permeability stratum and effectively reduce water cuts in the heterogeneous reservoir (Wang et al., 2021, 2022; Zou et al., 2020).

The positive effects of PMs on EOR have been extensively studied by many researchers, but most studies have focused on traditional microspheres such as polyacrylamide or silica

* Corresponding author. International Research Center for Renewable Energy, State Key Laboratory of Multiphase Flow in Power Engineering, Xi'an Jiaotong University, Xi'an, 710049, Shaanxi, PR China.
E-mail address: maochangliu@mail.xjtu.edu.cn (M.-C. Liu).

https://doi.org/10.1016/j.petsci.2023.12.013

(Gbadamosi, et al., 2018; Li et al., 2018; Masulli et al., 2022; Wang et al., 2023), and little attention has been paid to biomass microspheres. The PMs used for oil displacement and profile control are still in single varieties both in terms of bench-scale research and field tests (Wang et al., 2016; Zhou et al., 2019). Therefore, expanding the new type of biomass microspheres for EOR with controllable particle size, environmental friendliness and good deformability is one of the research directions to break the bottleneck of EOR in the future. The rapid development of biomaterials will open new frontiers for EOR (Ding et al., 2017; Pu et al., 2018a). For example, Zhang et al. (2022) has studied the effect of injecting biomass composite materials on the reservoir on profile control. Suspensions composed of micro-nano biological polymers also exhibit excellent performance in terms of improved rheology, oil–water interfacial activity, and stability (Li et al., 2023; Liu et al., 2019). These advances will facilitate the creation of new profile control and flooding agents—biomass microspheres. For this purpose, we have pioneered calcium alginate (CaAlg) microsphere EOR technology.

Sodium alginate (SA) can be extracted from the kelp of brown algae. It is easily obtained, cheap, and environmentally friendly. SA is an anionic polysaccharide mainly produced from marine brown algae and is a copolymer of 1–4 linked-β-D-mannuronate (M) and α-L-guluronate (G) homopolymeric blocks (Hecht and Srebnik, 2016). The main advantage of the alginate polymer is its easy preparation via ionic cross-linking with multivalent metal ions without the need for toxic chemicals or harsh conditions. The mechanism of gelation has been accepted as an egg-box model for years (Jay and Saltzman, 2009; Parekh et al., 2011). The carboxyl groups of two different alginate chains coordinate the metal ions between them, thus leading to an egg-box appearance (Cui et al., 2022). The high molecular weight of alginate polymer can increase the viscosity of fluid and steric hindrance introduced by the G unit around the carboxyl group (Zhao et al., 2020). Electrostatic repulsion between the charged groups on polymer chains further enhances the rigidity of the chain (Cui, et al., 2022; Zhang et al., 2018). The viscosity of the working fluid and the rigidity of the alginate polymer ensure the basic demand for oil control and displacement process. Based on the works of predecessors, this work of has discussed the modulation of phacoemulsification power, and put forward a convenient scheme for microsphere size regulation on the foundation of the power modulation adjustment to match porous media with different pore geometry. Furthermore, in order to improve the interface properties between oil-EOR fluid–rock surface, the CaAlg microspheres were modified with the very common surfactant SDS. In view of the toxicity of SDS, only a small amount of compounding was performed in this study despite the wide application of SDS. SDS can strongly interact with alginate, and the formation of these complexes can tune the properties and functions of microspheres, thereby positively affecting drug delivery, oil–water separation, and the food industry.

Reactive polymer alginate (M_w = 24,000–25,000) provides reaction zones for W/O emulsion ionic crosslinking process. The monodisperse CaAlg sphere fluid has good sphericity and shows high viscoelasticity and other rheological behavior. Besides, combining small amounts of SDS improves the interfacial properties (such as wettability and interfacial tension) between rock formations, working fluids, and the three phases of oil, thereby improving the capillary force.

Thus, a novel polymer fluid made of CaAlg/CaAlg-SDS microspheres and brine was successfully synthesized. Interestingly, the introduction of SDS may form the cross-linking between molecular chains due to the interaction of intertwined or hydrogen bonds with the gel network, thus affecting the rheological behavior of microfluidics (Bilici et al., 2021). More importantly, the relationship between oil displacement efficiency, rock surface, and injected fluid was revealed via classical core flooding and nuclear magnetic resonance (NMR) tests. The CaAlg-SDS microspheres achieve EOR by optimizing both micro and macro displacement efficiency. The former is influenced by capillary forces, which entrap oil within the reservoir and mainly a function of IFT and wettability while the latter is associated with rheological characteristics. Increasing the capillary number allows trapped oil to flow easily through the reservoir, while augmenting the viscosity of the injection fluid decreases the mobility ratio (Yakasai et al., 2021).

The results in oil–rock–fluid interactions on platform proved that CaAlg-SDS was favorable for oilfield practices where conventional PMs may show challenges. To the best of our knowledge, there is little research on biobased microspheres used in the petroleum industry, especially for EOR. The new insights can provide some reference on the synthesis of other polymer fluid employed in EOR. Their low cost, environmentally friendly nature, and biodegradable biomass are expected to add green features to tertiary recovery.

2. Experimental

2.1. Materials

Sodium alginate (SA), calcium chloride anhydrous ($CaCl_2$), lauryl sodium sulfate (SDS), mineral oil, Span 80, Tween 80, ethanol, and isopropanol were obtained from Sinopharm Group (Holding) Co. Ltd. Fluorine oil and kerosene were purchased from Shanghai Yadu Lubricants Co. Ltd. The brine was simulated formation water with the ionic composition exhibited in Table 1. Artificial core plugs were cemented quartz cores and their relevant parameters are summarized in Table 2. The type of pores in the artificial core is mainly intergranular pores, the permeability is about 15 mD, the pores are small and the roar is fine, which can basically reflect the situation of real core.

2.2. CaAlg/CaAlg-SDS microspheres and EOR fluid preparation

CaAlg or CaAlg-SDS microspheres with controllable size were prepared by an emulsification ionic crosslinking method, illustrated in Fig. 1(a), that was modified from the work of Garcia et al. (2017). The key distinction of this work from the previously reported synthesis methods is that the volume ratio of the water phase and the oil phase is always maintained at 1:2, and all emulsions were prepared using ultrasonic emulsification (SONICS, Model VC 750, rated power: 1 kW, amplitude: 0–100%) instead of other mechanical emulsification processes. Manipulation of the ultrasonic treatment process will facilitate the aim of controlling sphere size easier to implement. In a typical synthesis, as the disperse phase, SA solution (92.6 mM) was first hydrolyzed in 40 mL of water containing 0, 4, 8, and 12 mM SDS, respectively. Meanwhile, the continuous phase solution consists of mineral oil containing 5% (v/v) of Span 80, followed by ultrasonication treatment for 30 s (output power: 800 W, amplitude: 80%). Apparently, Span 80 was used here to emulsify incompatible water and oil phases into a uniform emulsion. Then the disperse phase was added and the mixture was emulsified by ultrasonic wave for 2 min at 800 W

Table 1
Ionic composition of the mineralized water.

Composition	Na^+	Mg^{2+}	Ca^{2+}	SO_4^{2-}
Concentration, mg/L	23,660	2340	3460	10,540

Table 2
Parameters of the cores used in core flooding experiments.

Core No.	EOR fluid	Length, cm	Diameter, cm	Air permeability, mD	Porosity, %	Pore volume, cm^2
1	CaAlg	4.76	2.50	14.12	16.17	4.14
2	CaAlg-4 mM SDS	4.85	2.50	13.54	16.20	3.85
3	CaAlg-8 mM SDS	4.64	2.50	12.58	15.92	4.56
4	CaAlg-12 mM SDS	4.91	2.50	13.23	15.32	4.69

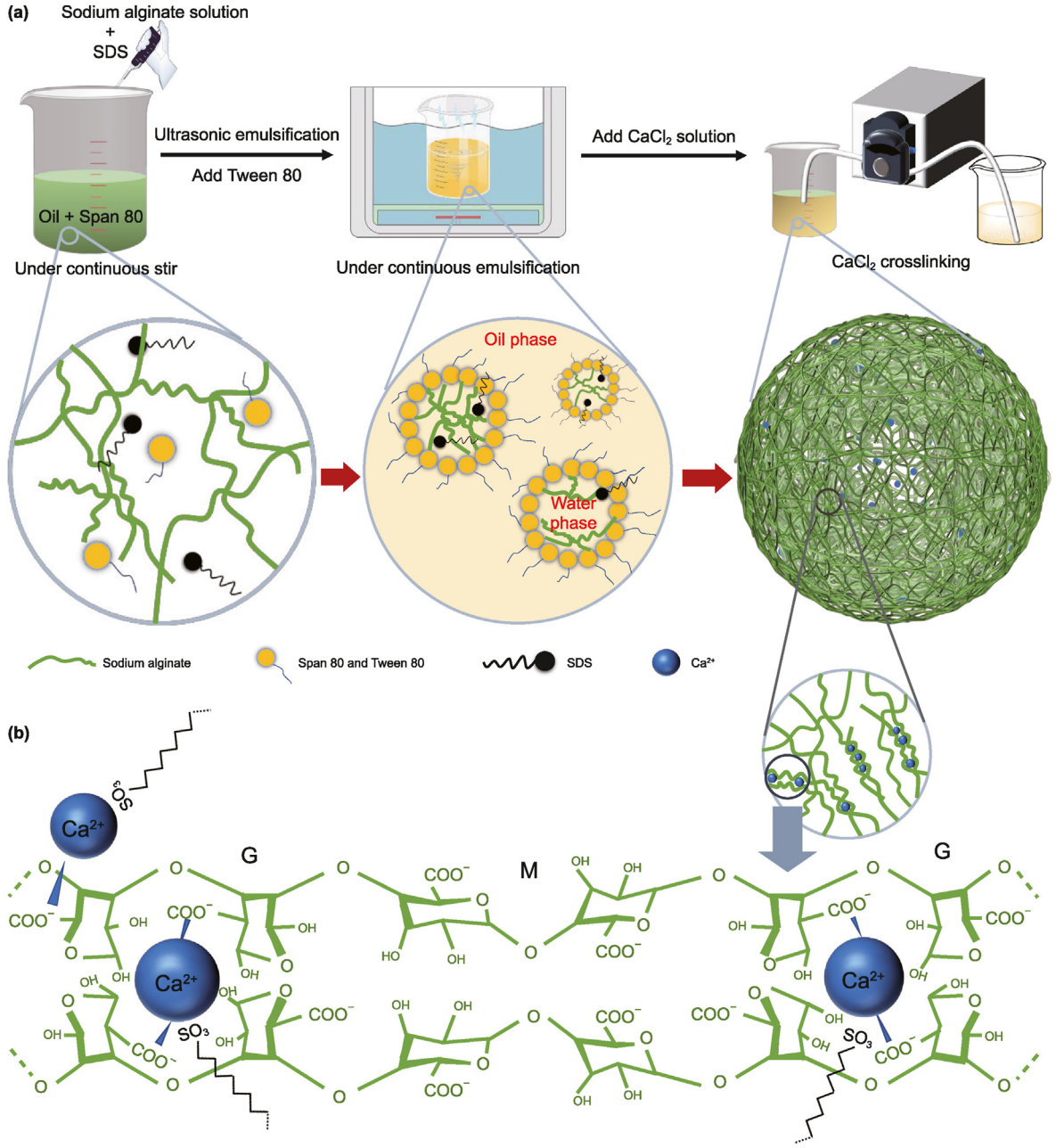

Fig. 1. Schematic illustration of the preparation process (**a**) and polymerization structure mechanism (**b**) for the microspheres (M: 1–4 linked-β-D-mannuronate, G: α-L-guluronate homopolymeric blocks).

power until it appeared homogeneous. After this step, 5 mL of an aqueous solution with 30% (v/v) Tween 80 was added to the W/O emulsion, and ultrasonic emulsification was continued at the same power for 1 min. After achieving a uniform mixture, the disperse phase was ionically cross-linked to form microspheres by adding 20 mL of a 700 mM $CaCl_2$ solution at 3 mL per minute while stirring at 800 rpm. Due to the addition of Tween 80, the W/O emulsion can continue to stabilize in ionic crosslinking and prevent the emulsion from delamination or precipitation.

After dripping, the solution was mixed for 3 min, treated with

50 mL isopropyl alcohol to solidify the microspheres for 3 min, and then centrifuged for 5 min at 4000 rpm. After removing the supernatant, the microspheres were washed in the same way twice in the same volume of anhydrous ethanol. This results in a sample of solidified microspheres that are then used for the following various characterization tests. At this point, polar functional groups on the polymer chains of microspheres form hydrogen bonds with bound water, and free water is still bound to the network structure of the sample. The resulting sample was placed in simulated formation water at a certain ratio, and functional tests, such as displacement test, were carried out in the follow-up experiment. This results in an EOR agent—CaAlg/CaAlg-SDS microsphere fluid, hereafter we collectively refer to microfluidics.

2.3. Morphology and microstructure characterization

The morphological analysis of CaAlg/CaAlg-SDS microspheres was performed by using a JEOL 7800F scanning electron microscope (SEM). Marvin nanometer size and potential analyzer was used to determine the particle size and zeta potential distribution of the microspheres in simulated formation water and deionized water. Fourier-transform infrared (FT-IR) spectra were recorded on a Bruker VECTOR-22 IR spectrometer. The XPS by UHV Analytical System Multichamber (Specs, Germany) was used to study the surface composition and changes of chemical properties of alginate and alginate-based composites before and after the SDS modification.

2.4. Hydrolytic and thermal stability characterization

The Setsis 1200 instrument was used to test thermal stability. The gel microspheres were heated in the N_2 atmosphere, with a flow rate of 20 mL/min, in the temperature range of 25–600 °C, with a heating rate of 10 °C per minute. In order to further evaluate the hydrolytic thermal stability, the microsphere samples were immersed in simulated formation water and heated to 100 °C for six days. The morphology and particle size changes were characterized by the experimental methods described in the preceding section. Besides, the transition gradient unit (TGU) was used to evaluate the crosslinking strength of gel microspheres with the transition pressure method proposed.

2.5. Rheological behavior measurement

To measure the rheological properties of the EOR fluid composed of CaAlg/CaAlg-SDS microspheres with 2000 mg/L, a visual rheometer (MCR302, Anton Par) with a DG42 rotor under the same steady shear model was used to test all samples. The shear rate was altered from 0 to 200 s^{-1}. Moreover, dynamic viscoelasticity tests of samples of the solidified microspheres, e.g., elastic modulus (G'), viscous modulus (G''), complex viscosity (η^*) were performed by the same instrument with a parallel plate (PP25) in ambient conditions. The gap size was set to 1 mm, and all samples tested were trimmed as needed so that they did not spill over when compressed. The strain was 0.5% and the angular frequency was in the range of 0.1–100 rad/s. Besides, static viscoelastic (creep behavior) tests were performed on the samples using the same rheometer (at 0.5% strain). A 1 kPa stress was initially applied to the sample, and the stress was discharged after 0.5 s. After 0.5 s, the sample recovered its original shape, thus characterizing the properties of creep.

2.6. Test of properties between different phases in oil–rock–fluid system

2.6.1. Interfacial tension (IFT) and hydrophilicity

Investigation of the impact of microspheres on the water/oil immiscible two-phase system was controlled via the addition of each agent by desired concentrations to the brine. The pendant drop method was adopted to obtain IFTs between the microfluidic (2000 mg/L) and kerosene. The IFT between the kerosene and test fluid could be automatically measured and recorded from an optical tensiometer attached to an image capture device. The same instrument was used to characterize the hydrophilicity of the CaAlg/CaAlg-SDS microspheres. Specifically, the sample powder was pressed into tablets by a tablet press, and then, the saline was dropped onto the sample pieces via the same hanging drop method. After the droplet stabilized for 5 s, the hydrophilicity was evaluated by a drop shape analyzer.

2.6.2. Wettability alteration in oil–rock–fluid system

Mathematically, wettability is a measure of the contact angle between two immiscible fluids and a solid surface due to intermolecular attractions (Yakasai et al., 2021). The contact angle between the microsphere fluids (2000 mg/L) and the rock slices in the oil matrices was determined using the same pendant drop method. The rock slice was immersed vertically and on a slant into the oil phase fluid, respectively. The rock was tilted into the oil phase at a certain angle to observe the contact angle change; it can reflect wetting hysteresis. The experimental diagram is shown schematically in Fig. 2.

2.7. Core displacement and nuclear magnetic resonance (NMR) experiments

The experiments were conducted using apparatus simplified in Fig. 3. The experimental procedures are as follows: (1) Artificial cores were first saturated with brine and fluorine oil to simulate the initial state of the porous medium. (2) After standing for 24 h to simulate the aging of saturated oil in the reservoir, brine was injected into the cores to achieve secondary oil recovery via water flooding (WF) until no oil was produced. (3) The microfluidics at 2000 mg/L were then introduced to initiate microfluid flooding (MF) and terminated until one pore volume (PV) injection was completed. (4) Subsequent water flooding (SWF) was performed

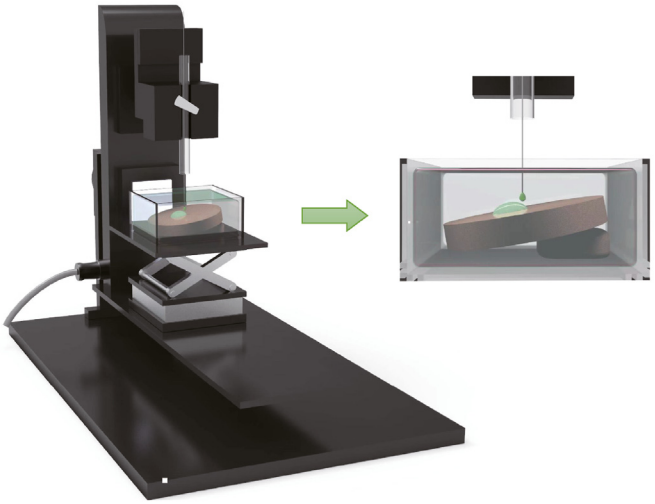

Fig. 2. Experimental diagram of wettability alteration in oil–rock–fluid system.

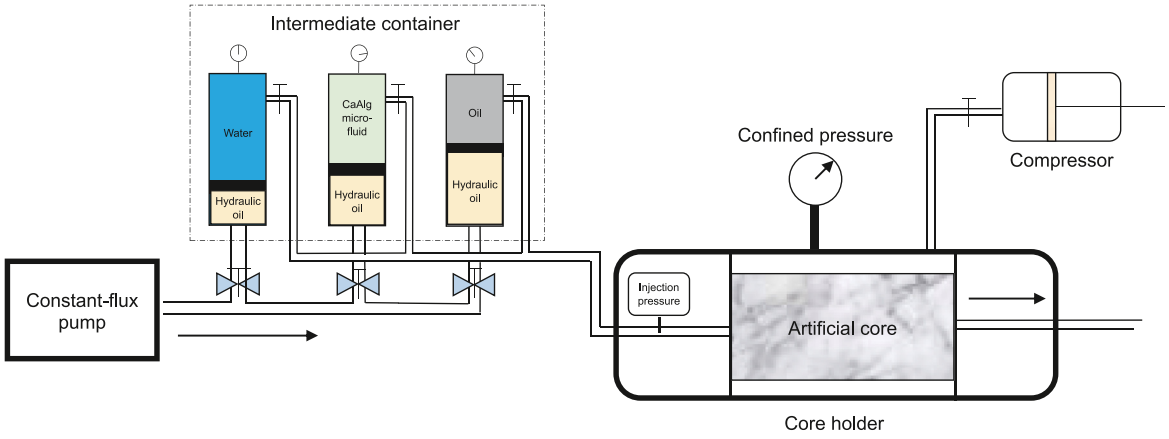

Fig. 3. Experimental diagram of core displacement device.

again until the injection pressure plateaued. The above flow rates were 0.1 mL/min and the differential pressure in the whole process was recorded. After the displacement was completed, the core was divided into three parts: entrance, middle, and exit according to the flow direction. The permeabilities of the three parts were also measured.

To estimate the profile control performance of microfluidics, changes in the injection pressures of cores Nos. 1–4 were evaluated; the corresponding resistance coefficients (F_R), residual resistance factor (F_{RR}), and plugging rate (η) were calculated.

$$k = \frac{Q\mu L}{A\Delta P_w} \tag{1}$$

$$F_R = \frac{\lambda_w}{\lambda_n} = \frac{k_w/\mu_w}{k_m/\mu_m} = \frac{\Delta P_m}{\Delta P_w} \tag{2}$$

$$\eta = \frac{k_{w1} - k_{w2}}{k_{w2}} \tag{3}$$

$$F_{RR} = \frac{k_{w1}}{k_{w2}} \tag{4}$$

where Q is the displacement flow rate, mL/s; L is the length of the porous medium, cm; A is the cross-sectional area, cm^2; μ is the fluid viscosity, mPa s; ΔP_w is the injection pressure of water flooding, MPa; ΔP_m is the injection pressure of fluidic microspheres, MPa; k_{w1} and k_{w2} are the initial and final permeability values, μm^2 (Dai et al., 2017).

Corresponding to the above displacement process, NMR tests were implemented to obtain the T_2 relaxation time spectra and images at each step to reflect characteristics of different fluids that flow in cores Nos. 1–4. The absence of hydrogen in fluorine oil leads to a subtle NMR signal, and a relatively strong signal was observed for water. Thus, the T_2 relaxation time spectra and images reflect the water saturation in different pores and contribution of different pores to the recovery degree (Di et al., 2017).

3. Results and discussion

3.1. Physicochemical properties of microfluidics

Molecular chains containing carboxyl SA will lead to instant contact with Ca^{2+} on the G unit, causing Ca^{2+} exchange and gelation. Synthesis of the W/O microemulsion for this type of ion exchange and crosslinking produces a gel network and a reaction zone (Fig. 1(a)). From Fig. 1(b), a G cell stack forms the characteristic egg-type space structure. SEM micrographs (Fig. 4) show that the degree of sphericity of the sample is high, though the surface of the microspheres is rough. The as-prepared CaAlg has well-dispersed microspheres with an average particle diameter of about 1.25 μm (Fig. 4(a)). Furthermore, it can be observed from Fig. 4(b)–(d) that the hydrophobic alkyl tail was incorporated into the CaAlg microspheres by compounding SDS making the surface of the composite microspheres more densely cross-linked, the sphere size showed no obvious change, and the dispersity was also superior. This has been caused by GG fragment that introduces steric hindrance around the carboxyl group, which makes the microspheres disperse well, and the electrostatic repulsion between the charged groups on the polymer chain further reduces agglomeration. The inset in Fig. 4(a) shows that the zeta potential value of pure CaAlg microspheres was −25.6 mV, whereas the potential of modified microspheres was reduced to −33.7 mV (CaAlg-12 mM SDS). Since CaAlg-SDS microspheres have more edge groups on the surface that can ionize carboxyl and sulfate, the potential value of microspheres became more negative with the increase in SDS modification, indicating that the stability of the microsphere dispersion system was improved. The average potential value of microspheres in simulated formation water is shown in Table 3. Therefore, the surface negative charge in Table 3 is slightly weakened. Bivalent cations can interact with negatively charged sites on the surface of calcium alginate microspheres. When calcium ions adsorb onto the surface of the microsphere, they can neutralize part of the negative charge on the surface of the microsphere and reduce the negative charge density on the surface of the microsphere. Besides, changing the ultrasonic power facilitates particle size regulation to match different micropores in porous media. The result is shown in Fig. 5.

FT-IR was used to further detect the surface functional groups of the CaAlg/CaAlg-SDS (Fig. 6(a)). The peaks at about 1623 and 1436 cm^{-1} were associated with the asymmetric and symmetric stretching vibrations of the carboxyl groups, respectively; while the two absorption bands at about 1093 and 1025 cm^{-1} belonged to the C–O–C groups of the saccharide structure. Besides, asymmetric stretching modes of the sulfate group of the SDS molecule gave two peaks at 1285 and 1250 cm^{-1}. SDS-modified microspheres showed two sharp peaks at 2917 and 2850 cm^{-1}, which result from the asymmetric and symmetric stretching vibrations of $-CH_2$ groups of the SDS molecule. This signal showed an interaction between CaAlg and SDS. Fig. 6(b)–(d) show the XPS spectra of C 1*s*, S 2*p*, Ca 2*p*, and O 1*s* for CaAlg with different SDS addition. The intensity of the C 1*s*

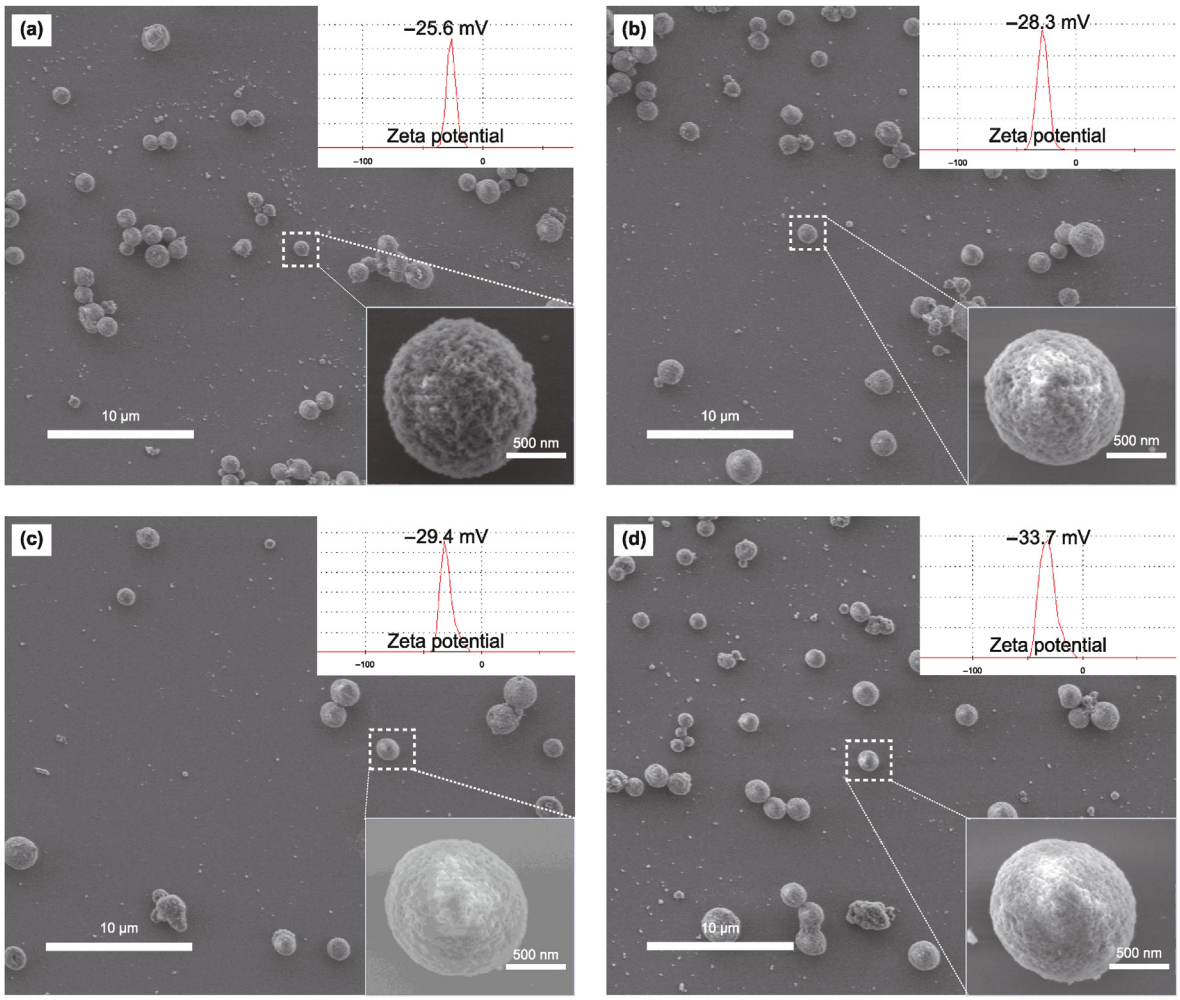

Fig. 4. SEM images and zeta potential of CaAlg (**a**), CaAlg-4 mM SDS (**b**), CaAlg-8 mM SDS (**c**), and CaAlg-12 mM SDS (**d**).

Table 3
Mean zeta potential of microspheres in simulated formation water.

Type	Mean zeta potential, mV
CaAlg	−18.62
CaAlg-4 mM	−21.37
CaAlg-8 mM	−20.54
CaAlg-12 mM	−24.17
Formation water	1.68

signals in CaAlg-12 mM SDS is higher than that in CaAlg, indicating that C 1*s* signals are heightened with the increase in the number of long carbon chains in SDS-modified microspheres (Fig. 6(b)). Additionally, for the CaAlg-SDS composite microspheres, the peak at a binding energy of 168.6 eV can be attributed to the sulfate group of the SDS molecule (Fig. 6(c)). These also demonstrate SDS was anchored on the surface of the microspheres by adding different amounts of SDS. As shown in Fig. 6(d), the typical Ca 2*p* core-level spectra of alginate gels can be fitted by two peaks at binding energies of around 350.6 and 347.0 eV.

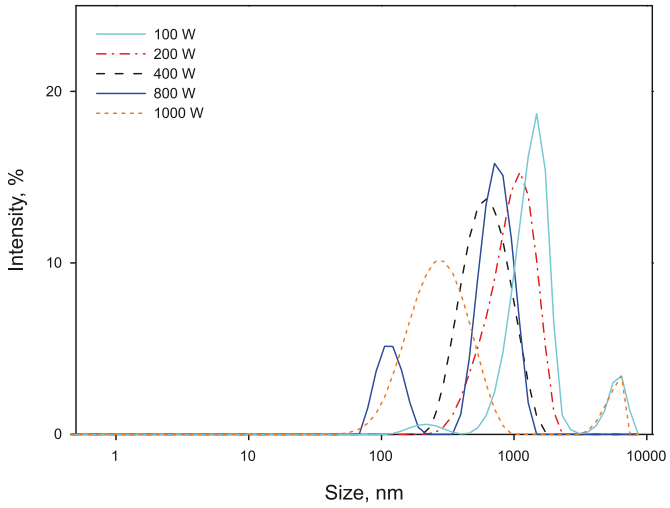

Fig. 5. Size distribution of CaAlg microspheres prepared under different ultrasonic power (other conditions remain unchanged).

3.2. Hydrolytic and thermal stability

The thermogravimetric analysis (TGA) results of the microspheres are shown in Fig. 7. The curves were found with three steps of weight loss in the range of 25–600 °C, including dehydration of free and bound water (< 90 °C), decarboxylation (90–220 °C), and degradation of some polymers (> 220 °C). From the second stage

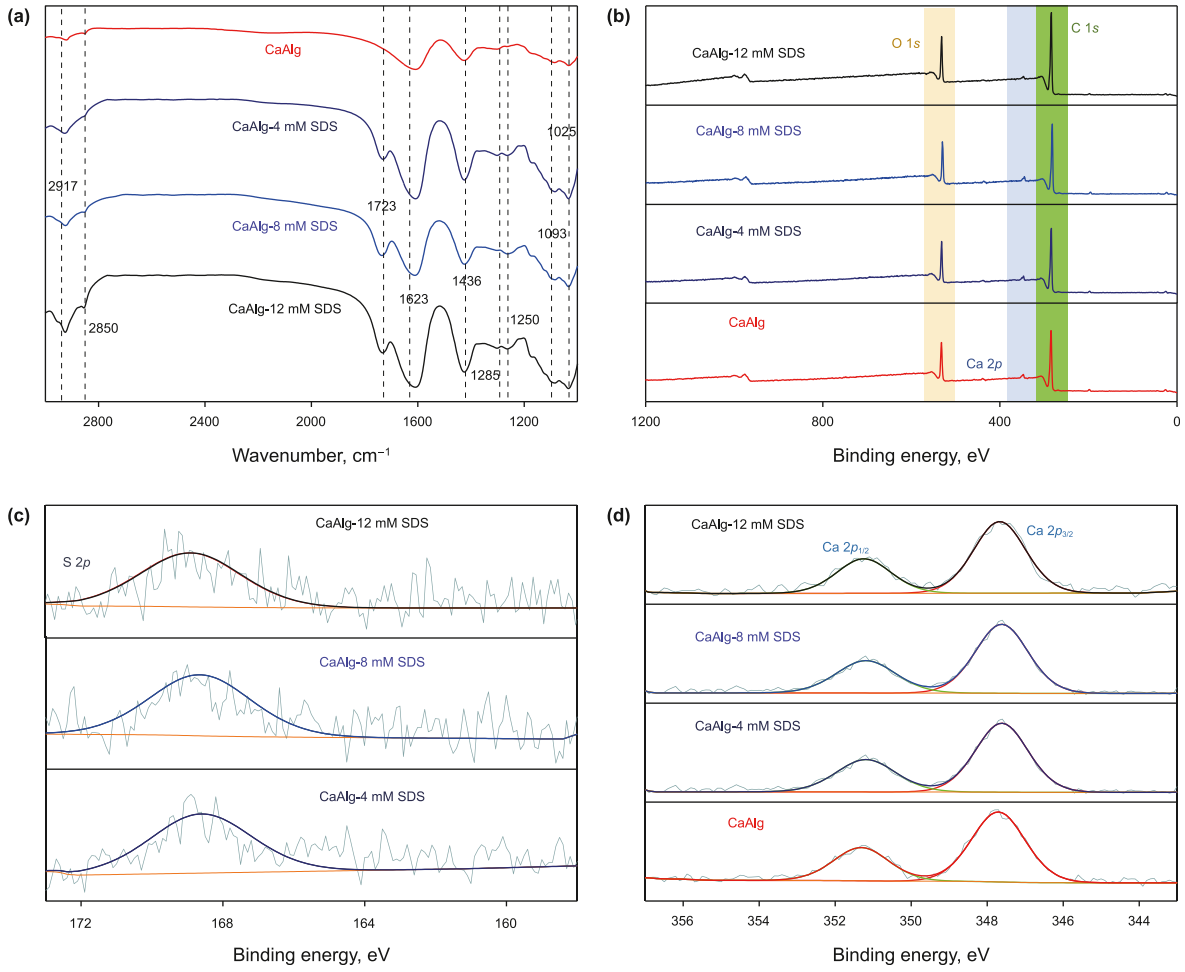

Fig. 6. FTIR (**a**) and XPS (**b**, **c**, **d**) spectra of CaAlg and CaAlg with different SDS content.

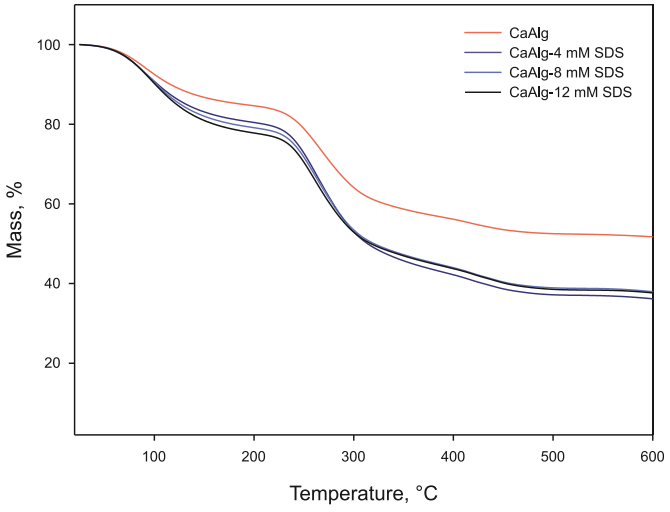

Fig. 7. TGA curves of CaAlg and CaAlg with different SDS content.

onwards, the weight losses of CaAlg were significantly reduced than that of CaAlg-SDS, indicating alkyl group stripping and sulfuric acid group decomposition in CaAlg-SDS. The weight loss of the microspheres at 100 °C is less than 10%, which indicates that the temperature resistance of the microspheres basically meets the temperature requirements of most oil reservoirs in China.

Time-course expansion ratio of the microspheres in the brine is given in Fig. 8(a) and the particle size distribution of the microspheres six days later is shown in Fig. 8(b). Clearly, the expansion of microspheres increased quickly in the first day and then this increment became less evident and eventually tended to plateau. Moreover, it was found that the expansion of microspheres decreased with the increment in SDS at the same hydration time.

$$E = \frac{D_2 - D_1}{D_1} \tag{5}$$

where E is the expansion of microspheres; D_1 and D_2 are the average diameters of microspheres before and after expansion, respectively.

In principle, higher crosslinking strength usually slows the swelling rate of the polymer, because the increase in crosslinking points will necessarily inhibit swelling. CaAlg-12 mM SDS with relatively slow swelling shows the largest crosslinking strength, and the particles still maintain good sphericity even if they are hydrated in 100 °C brine for a long time (Fig. 8(c)), which also reflected that a small amount of Na^+ in formation water is insufficient to degrade the microspheres.

To further evaluate the crosslinking strength of the microspheres, the transition pressure is obtained by plotting pressure against flow rate and TGU value (Eq. (6) (Smith, 1989). Note that the TGU value is the ratio of the resistance to flow of a gel to that of

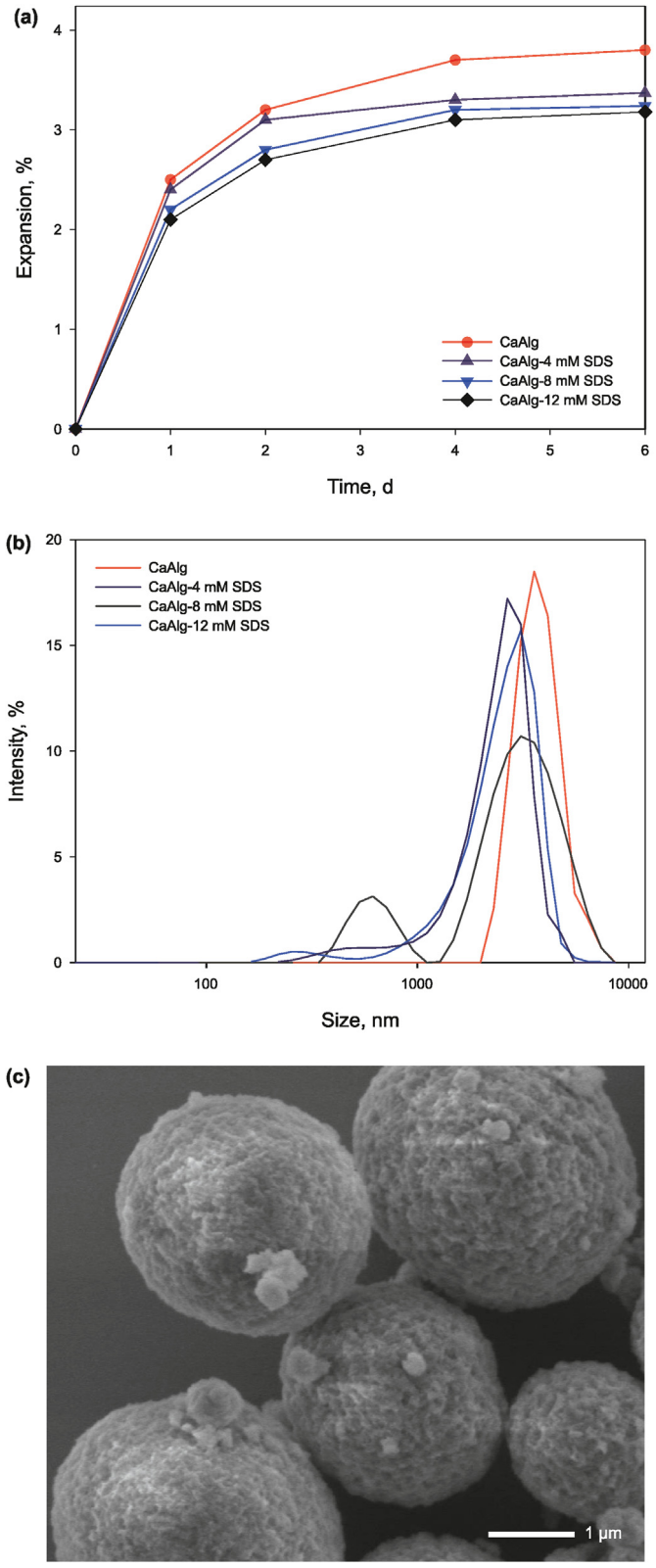

Fig. 8. (**a**) Expansion changes of microspheres in simulated formation water; (**b**) Size distribution of microspheres after six days; (**c**) CaAlg-12 mM SDS morphology after six days of formation water aging at high temperature.

uncrosslinked polymer and is proportional to the strength of the gel microspheres:

$$\mathrm{TGU} = \frac{Q_p}{Q_g} \tag{6}$$

As shown in Fig. 9, the transition pressure also increased at higher SDS modification, indicating increased crosslinking points of the microspheres and enhanced strength of microsphere by combination with SDS.

3.3. Rheological behavior

The viscosity–shear rate relationship and shear stress–shear rate relationship for the microfluid composed of microspheres are given in Fig. 10(a). The flow velocity in the formation is actually low, especially in low shear rate fields, where microfluidics had a higher viscosity than those with brine used for secondary oil recovery. Thus, it has to be noted that meeting the basic mobility (λ) requirements of the microfluidic as a displacement phase during tertiary oil recovery. Higher viscosity displacement fluids can effectively reduce the oil flow mobility ratio and expand the swept volume (Eq. (7)).

$$M = \frac{\lambda_w}{\lambda_o} = \frac{k_w/\mu_w}{k_o/\mu_o} \tag{7}$$

where M is the mobility ratio; λ_w is the mobility of the displacing fluid (microfluidics); λ_o is the mobility of the displaced phase (oil); k_w and k_o are the permeability of the displacing phase and that of the displaced phase, respectively, μm^2; μ_w and μ_o are the viscosity of the displacement phase and that of the displaced phase, respectively, Pa s.

The flow curves for all microfluidics were approximately conformed to that of generalized Newtonian fluid models, but shear-thinning behavior existed in the high shear rate range—particularly CaAlg fluids reveal more conspicuous (Fig. 10(a)). The characteristics of curves are the result of changes in the morphology of the cross-linked spatial network under shear, based on this it can be inferred the introduction of SDS may form the cross-linking between molecular chains due to the interaction of intertwined or hydrogen bonds with the gel network, which intensified the flow stability. Since the attractive interactions between the hydrophobic segments (SDS carbon chain and copolymer chain) are not electrostatic, it can be theoretically deemed that this interaction

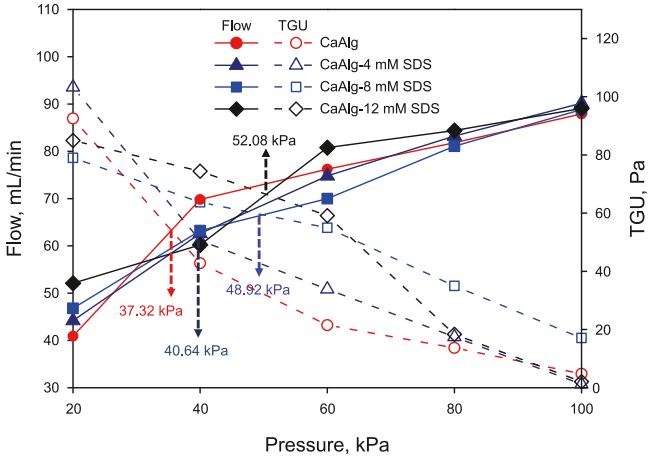

Fig. 9. Transition pressures of CaAlg-SDS microsphere systems.

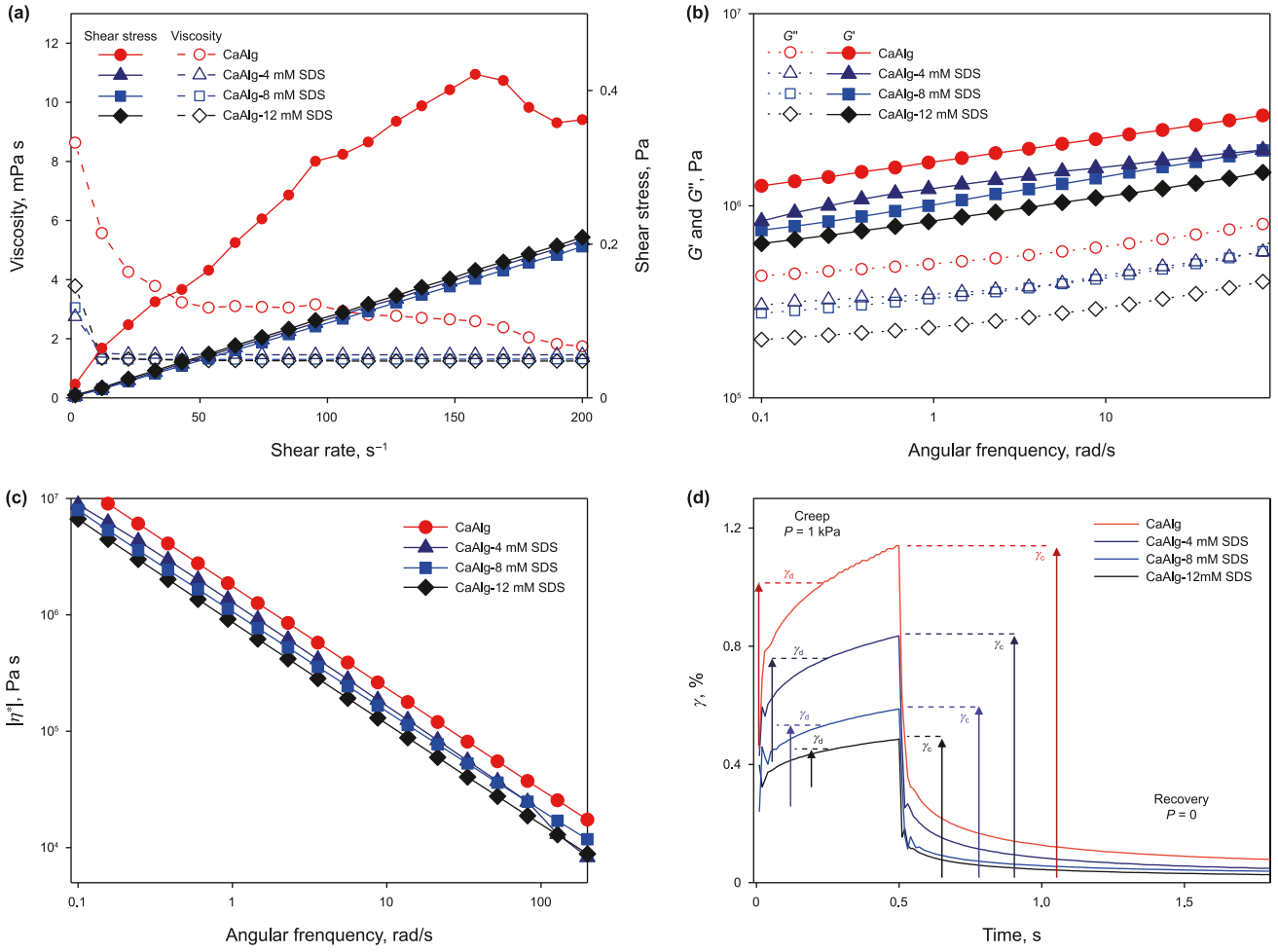

Fig. 10. (**a**) Viscosity (solid line) and shear stress (dash line) changes as a function of shear rate for different microsphere; (**b**) Storage modulus and loss modulus of different microspheres; (**c**) Complex viscosity changes of different microspheres; (**d**) Creep curves of different microspheres (creep and recovery).

induces a contracted conformation of the polymer chain. It could be further speculated lower viscosity values were obtained from the CaAlg-SDS fluid throughout the whole shear rate region, manifesting a smaller hydrodynamic dimension of the CaAlg-SDS chain compared to that of CaAlg (Bu et al., 2005, 2006).

Moreover, viscoelasticity is also a special rheological behavior in which the energy storage modulus (G') derives from the transient change of network chain conformation and thus is used to characterize elasticity. Generally, Fig. 10(b) displays a typical linear viscoelastic (LVE) modal, and the G' is rifely higher than the G'', suggesting that the viscous behavior of these four samples is greater than the elastic behavior in terms of viscoelastic performance. Notably, the G' and G'' of the microsphere system developed in this study is better than previously reported (Liu et al., 2021; Pu et al., 2018b; Zhang et al., 2022). Complex viscosity (η^*) can also be used to characterize the viscoelastic properties of the disperse system as a whole, the results are presented in Fig. 10(c). The value of complex viscosity ($|\eta^*|$) decreases as the oscillation frequency increases, indicating that the bulk structure is affected by the oscillation. This means a reduction in the hydrodynamic radius of the microspheres and a decrease in internal friction between microspheres in the dispersion system, resulting in reduced fluid resistance to flow. Since the collision between fluid molecules and particles will affect the trajectory of particles at a micro scale, especially in viscous fluids, particles are more affected by fluid viscosity. The so-called hydrodynamic radius refers to the average distance that small particles (such as microspheres) moving in the fluid are affected by the collision of fluid molecules in the fluid.

The results of the static viscoelastic test, i.e., the creep and recovery curves are depicted in Fig. 10(d). The creep behavior of samples was divided into three stages: (1) when a constant stress was applied to the sample, the strain curve appears initially a rapid steplike increase which is caused by the deformation of polymer chains by segmental motion. (2) Then a gradually decreasing slope of the strain curve can be observed and the process is retarded by the surrounding viscous continuous mass and the formation of intermolecular associations. This part occupied the largest proportion in the creep phase and the strain corresponding to this is defined as retardation strain γ_d. (3) Finally, the instantaneous elastic response appears with the removal of the applied strain and the delayed elastic response recovered gradually. Overall, the total creep strain γ_c is equivalent to the sum of the three contributions (Li et al., 2017). It can be seen from Fig. 10(d) that CaAlg showed higher γ_d and γ_c than the SDS-modified ones. In total, CaAlg-SDS has static and dynamic viscoelasticity that is lower than that of CaAlg, which can be attributed to the compacted conformation of the alginate chain induced by the screening of the electrostatic repulsions along the polymer chain by the compounding SDS. Thus, with the increase in SDS modification, the G', $|\eta^*|$ and γ are weakened, as demonstrated in Fig. 10(b)–(d), but still reflect good

elastic deformation ability. Similarly, the incorporation of the SDS non-polar carbon chain to the CaAlg copolymer chain also enhance this hydrophobic-hydrophobic interaction. The consequent increasing number of cross-linker points heightens the stiffness and Young's modulus in the microspheres. This also explains that the hydrodynamic size of the polymer decreasing with increasing SDS; the flow stability increases instead.

3.4. Properties between different phases in oil–rock–fluid system

3.4.1. IFT and hydrophilicity

The rheological behavior discussed above can improve the macroscopic displacement efficiency and deep profile control effect. Correspondingly, the microscope displacement efficiency is related to capillary forces which trap oil in the reservoir and mainly dictated by IFT and wettability, as described by Eq. (8):

$$N_C = \frac{v\mu_w}{\sigma_{ow}\cos\theta} \tag{8}$$

where N_C is the capillary number; v is the seepage velocity; θ is the contact angle; σ_{ow} is IFT between the displacing phase (water) and the displaced phase (oil).

More deeply, hydrophobicity is surface property which defines the surface energy and binding affinity of microspheres, and it is more or less a function of the extent of IFT reduction and wettability alteration (Yakasai, et al., 2021). Therefore, we first discuss the hydrophilicity/hydrophobicity of the microspheres themselves in this section basis on Fig. 11. Hydrophobic regions are introduced after SDS modification, which weakens the hydrophilicity of CaAlg to a certain degree, though it is still mainly hydrophilic. Accordingly, compared to brine, the addition of microspheres can reduce IFT—the modification of SDS can reduce IFT more significantly, although not much SDS was added in the synthesis process (Fig. 11). The IFT reduction mechanism of the O/W interface using microfluidics is governed by the adsorption of the microspheres at the interface whereas the adsorption of the microspheres at the interface is associated with the sphere hydrophobicity. For this, the modification of the microspheres by SDS non-polar tail chains improved the hydrophobicity of the microspheres, as well as the asymmetry of the macromolecules. Therefore, the microscopic mechanism may be the reduction of polarity difference, i.e., the surface energy, and the resulting migration of the existing interface.

3.4.2. Wettability alteration in oil–rock–fluid multiphase system

As stated previously, CaAlg itself is extremely hydrophilic. Next, to demonstrate the wettability alteration of rock slices immersed in the oil phase, we measured the contact angle of the microfluidic on the rock. The wetting state of reservoir rock is the ability of a fluid phase to dominate a solid surface in the presence of a second immiscible phase. In application, the wettability and IFT will lead to a change in capillary number (Eq. (8)). Whereas 0–90°, 90°, and 90°–180° indicate water-wet, intermediate wet, and oil-wet, respectively (Ghandi et al., 2019).

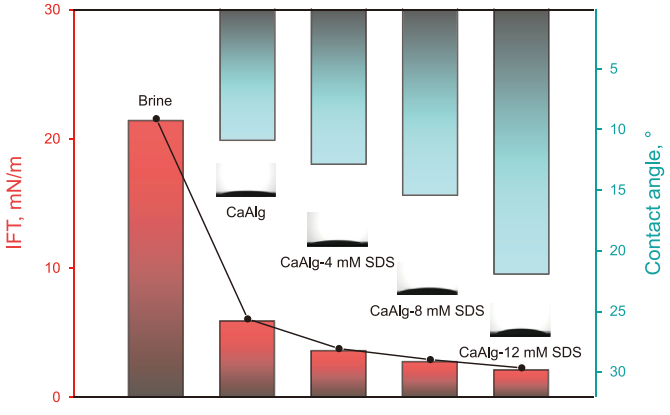

Fig. 11. IFT and hydrophobicity of CaAlg, CaAlg-4 mM SDS, CaAlg-8 mM SDS and CaAlg-12 mM SDS.

Fig. 12(a)–(e) represent the changes in the contact angle as a criterion of the wettability for the reservoir rocks after interaction with the microfluidics. The presence of the microspheres in the droplet reduced the contact angle as a result of altering wettability from initial oil-wet (116°) to water-wet and intermediate wet. Driven by electrostatic repulsion force between the spheres, microfluidic will spread along the solid surface and decrease contact angle. With an increase of SDS in composite microsphere, the wetting ability of the rock has been altered from a water wet (83°) to approximate intermediate wet (89°). This indicates that the modification by SDS does not fundamentally reverse the hydrophilicity of the solid surface of the microspheres and does not significantly affect the wettability change in the three-phase system.

It is well documented that when the wettability is neutrally or slightly water wet, the displacement efficiency is maximal (Shariatpanahi et al., 2016). Specifically, on the surface of the relatively hydrophilic rock, capillary forces drive water phase seepage when water displaces oil. In terms of Eq. (6), reducing the IFT or the wetting angle to nearly neutral wetting is conducive to increasing N_C, and then effectively improving the microscopic efficiency of oil displacement. After tilting the originally horizontal rock surface at a small angle, it can be seen that the oil–water–solid boundary does not move forward immediately. Deformations only occur at the oil–water interface and the variation of the wetting angle of fluid is not large ($\Delta\theta < 10°$), which still shows weak water-wet or near intermediate wet (Fig. 12(f)–(j)). In the process of one phase displacing another phase, the static wetting hysteresis phenomenon is not prominent, which is conducive to improving the micro displacement efficiency.

3.5. EOR property of microfluidics

3.5.1. Profile control performance

The injectivity, migration and plugging ability were evaluated through unsteady-state flooding experiments over the microfluidics. Fig. 13 reveals the relationship between the injection pressure and injection volume during the oil displacement processes of WF (I), MF(II), and SWF (III). It should be noted that due to the low permeability of the artificial core and poor connectivity, the pressure in the WF (stage I) was not low from the very beginning. Immediately after the end of the WF, the pressure suddenly increased sharply at the beginning of the MF (stage II). This increment indicates that the fluidic microspheres plugged throats of the reservoirs. In the core No. 1, the pressure of CaAlg fluid was more sensitive to the injection volume, that is, it increased most rapidly in the early stage II. This also implies that microspheres with higher elasticity may possess a more notable impact on sweep efficiency, as discussed in Section 3.3. In fact, the continually increasing pressure reflects an unstable flow status, indicating the microspheres blockage and retention does not reach the maximum if microspheres are continuously injected.

In the initial SWF (stage III), the pressures were still increased for a short time, indicating effective block of the pores, and then microspheres were forced forward through throats, resulting noticeable decrease in pressure value. This indicates that with the progress of SWF, the microspheres were constantly migrated and

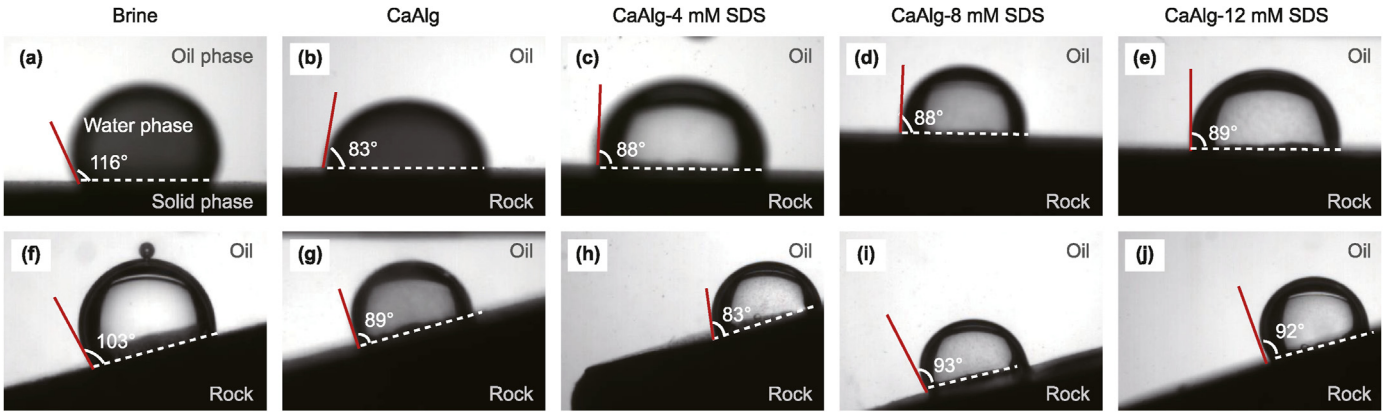

Fig. 12. Three-phase contact angle of CaAlg, CaAlg-4 mM SDS, CaAlg-8 mM SDS and CaAlg-12 mM SDS.

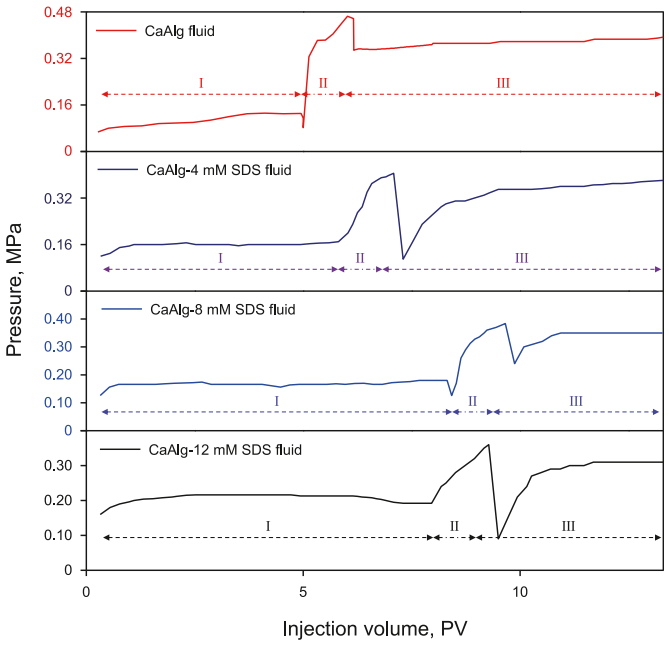

Fig. 13. Injection pressures of the different fluids under different cumulative injection volumes during water flooding (WF) (I), microfluidic flooding (MF) (II), and subsequent water flooding (SWF) (III).

wriggled into the core through their excellent elastic deformation ability and release injection pressure. As presented in Fig. 13, with the increase of SDS in the composite microsphere, the pressure drops at early stage III became more gently, which also reflects the changes in the viscoelasticity of microspheres by SDS from another aspect, and then affects the migration of microspheres in the porous medium. During the SWF, the pressure generally remained high. The pressure fluctuation during the late SWF was largely a result of alternative transportation and blockage of microspheres, that is, migration, plugging, elastic deformation, re-migration, and re-plugging, and so on (Pu et al., 2018c). In conclusion, the increasing injection pressure and the still relatively high SWF pressure indicate that the microspheres exhibit effective plugging behavior and match well with porous media. In order to further verify the injectability of microspheres, the permeability of the entrance, middle, and outlet parts of the core was analyzed. It was found that the permeability of each core along the flow direction increased. However, the increment was not large, and all were lower than the permeability of the core before injection. This indicates that a certain amount of microspheres accompanied by fluid migrated deep into the core to complete plugging (Fig. 14).

Although the four flooding experiments have shown good in-depth migration and plugging ability, it is worth noting that the cores No. 1 and No. 2 demonstrated higher pressure differential with regard to that of others. Thus, the CaAlg and CaAlg-4 mM SDS microspheres had better profile control capacity. These results were verified by the resistance coefficients (F_R), residual resistance factors (F_{RR}) and plugging rates (η), as presented in Table 4. Apparently, the η of fluids is positively correlated with static and dynamic viscoelasticity, whether it is G', creep strain γ, or other metrics. The results also show excellent rheological behavior, even at low concentrations, contributing to the microspheres fluid with satisfactory ability to promote macrodcopic displacement.

3.5.2. Recovery factor of remaining oil

Based on the spatial-temporal transformation theory of pore size and transverse relaxation time T_2 in NMR experiments, the core pore radius is proportional to T_2 value. More precisely, the correspondence between pore-throat radius and relaxation time is expressed as

$$\frac{1}{T_2} \approx \rho_2 \frac{F_s}{r} \tag{9}$$

where F_s is the pore dimensionless shape factor; ρ_2 is the relaxivity

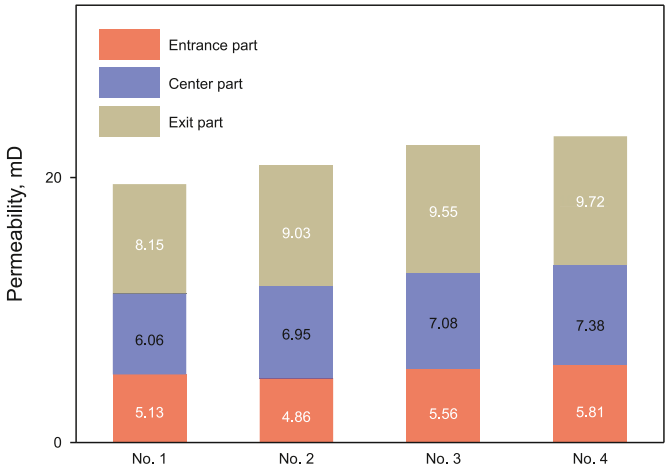

Fig. 14. Permeability distribution of different parts of the cores.

Table 4
Flow plugging ability of EOR fluids of different concentrations.

Core No.	Fluidic microspheres	ΔP_w, MPa	ΔP_m, MPa	ΔP_{sw}, MPa	η, %	F_R	F_{RR}
1	CaAlg	0.12	0.46	0.40	70.06	3.83	3.34
2	CaAlg-4 mM SDS	0.15	0.41	0.39	61.54	2.73	2.60
3	CaAlg-8 Mm SDS	0.16	0.38	0.37	56.76	2.38	2.31
4	CaAlg-12 mM SDS	0.19	0.36	0.34	44.13	1.89	1.79

of transverse surface, μm/ms; r is the pore radius, μm; and T_2 is the relaxation time, ms. The area surrounded by signal amplitude and relaxation time reflects the volume of fluid in the different pore size intervals, thus, it can be seen in the NMR result curve (Fig. 15) that the fluid was mainly distributed in the pore size of 0.1–100 ms. Then in this subsection, T_2 values of less than 10 ms, 10–50 ms, and greater than 50 ms were defined as micropores, mesopores, and macropores, and the corresponding pore-throat radii are less than 4.3 μm, 4.3–21.5 μm, and greater than 21.5 μm, respectively.

As presented in Fig. 15, with the injection of microfluid, the peak point of T_2 spectrum both shifted slightly to right, indirect indicating that the microspheres had a certain profile control effect, as mentioned in previous section. What's more, the peak areas of the T_2 spectra in four cores after MF and SWF were smaller than saturated water stage and larger than saturated oil stage, indicating that the oil content reduced and the microfluid had positive effect on EOR. Among them, the T_2 spectra of SWF in Fig. 15(a) and MF in Fig. 15(b) increased obviously than those of the WF stage, and the spectra of MF and SWF stages in cores No. 3 and No. 4 were slightly improved (Fig. 15(c)–(d)). Apparently, the area difference between the two curves represents changes in fluid volume. Accordingly, the recovery factor f_r in different occurrence states can be given as follows

$$f_r = \frac{S_i - S_o}{S_w - S_o} \tag{10}$$

where S_w, S_o, and S_i are the areas enclosed by T_2 spectrum curves of the initial saturated water, oil-saturated, and displacement stages within a certain range, respectively.

The recovery factor results at various ranges are compared in Table 5 and Fig. 16. Firstly, the results after WF are basically similar since cores Nos. 1–4 were produced from the same template and materials, for example, the WF efficiencies are both 40%–50%. As injected water preferred to flow through the dominant channels, which led to low sweep efficiency at low permeability sublayers. Naturally, there was still a considerable amount of undisturbed bound-state remaining oil exists in the cores. At this time, profile control treatment was needed. In the stage of MF, Fig. 16(a) shows the recovery degree of micropores in core No. 1 is negative. It is

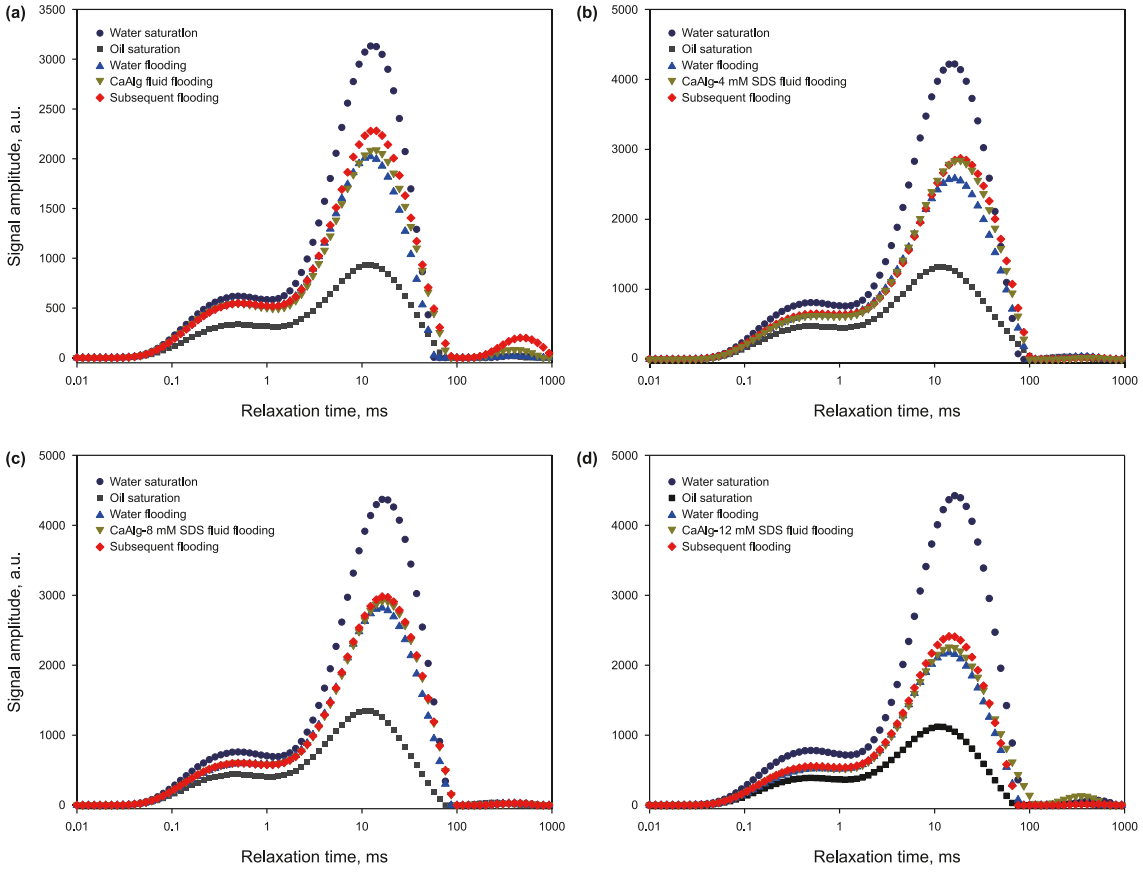

Fig. 15. Changes of T_2 spectra during microsphere displacement with concentration of 2000 mg/L of CaAlg (**a**), CaAlg-4 mM SDS (**b**), CaAlg-8 Mm SDS (**c**), and CaAlg-12 mM SDS (**d**).

Table 5
Oil recovery of EOR fluid in different cores.

Core No.	Recovery factor at different stages, %			Relative recovery factor different pores, %			Total recovery factor, %
	WF	MF	SWF	Micropores	Mesopores	Macopores	
1	43.72	11.31	18.75	53.18	75.59	94.14	73.78
2	46.36	22.13	12.25	50.73	85.97	81.31	80.74
3	49.24	8.53	7.32	52.56	64.84	78.86	65.09
4	48.56	9.26	5.50	51.38	66.53	63.26	63.32

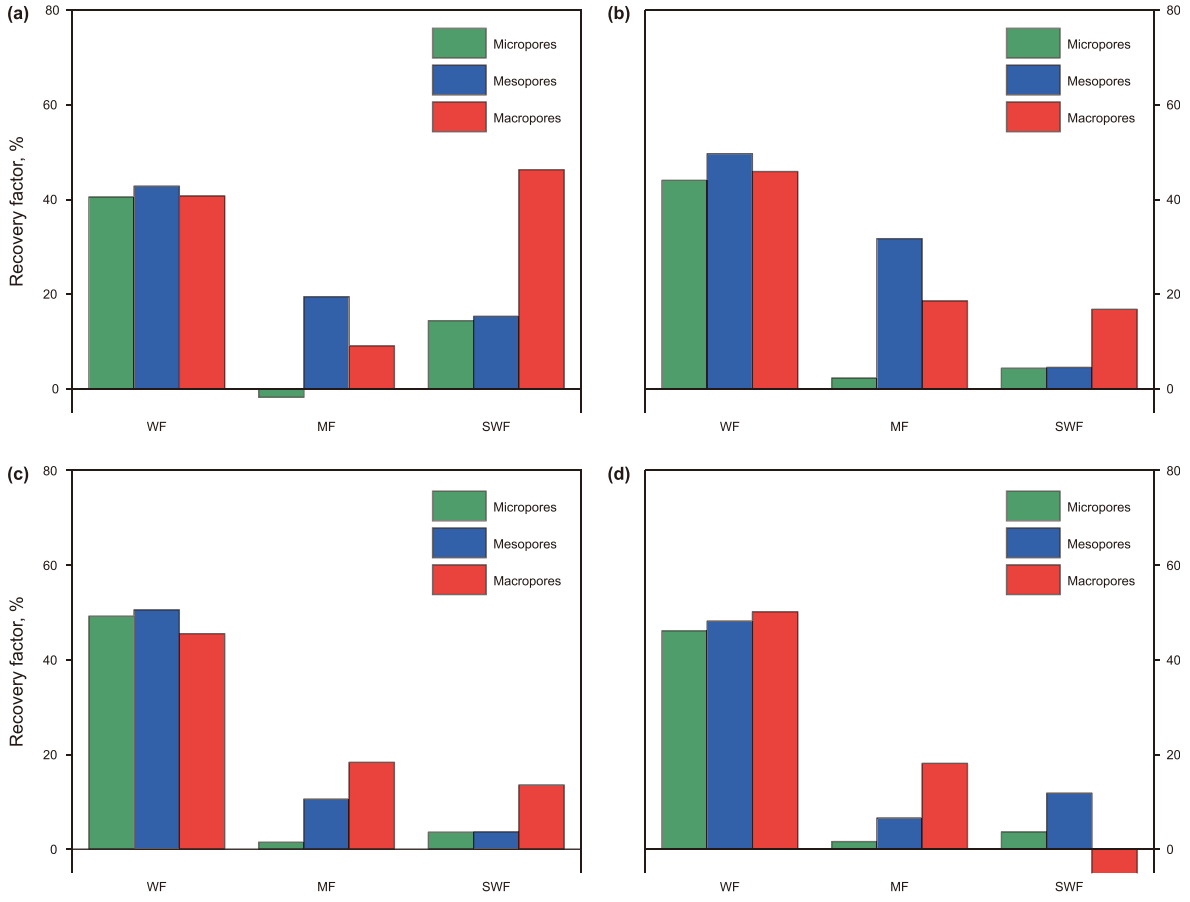

Fig. 16. Comparison of recovery factors at different stages and pore ranges. (**a**) CaAlg; (**b**) CaAlg-4 mM SDS; (**c**) CaAlg-8 mM SDS; (**d**) CaAlg-12 mM SDS.

inferred that CaAlg microspheres first enter the high permeability zone to form efficient plugging and at the same time squeeze part of the oil into micropores. Furthermore, core No. 1 exhibits the highest SWF efficiencies across all three types of pores, signifying the redirection of subsequent injected water to low permeability zones with high oil saturation, resulting in widespread oil displacement and ultimately contributing to a greater cumulative oil recovery rate of 73.78%. In addition, for the unmodified microspheres, the degree of micropore mobilization is not weak in SWF (Fig. 16(a)), which reflects the excellent elastic deformation ability. Therefore, the EOR mechanism of CaAlg fluid can be partially illustrated through the differential pressure profile, as discussed in Section 3.5.1.

As listed in Table 4, the MF efficiency was greatest in core No. 2 accounting for 20.13%, while Fig. 16(b) displayed that the oil production of MF was most prominent in the mesopores. Overall, the large contribution of mesopores helps the total recovery factor reach 80.74%. The primary reason for the greatest recovery factor of core No. 2 can be attributed to two factors. Firstly, the CaAlg-4 mM SDS fluid exhibits superior microscopic oil displacement capacity owing to its excellent interfacial performance, compared to CaAlg fluid, as validated in Section 3.4. Secondly, the injection of CaAlg-4 mM SDS microspheres also leads to enlarging macroscopic sweep volume, redirecting subsequent fluids towards previously untapped regions containing residual oil. By contrast, the oil recovery factor of roughly 9% was achieved of MF in cores No. 3 and No. 4, while that in the SWF stage was almost negligible (Fig. 16(c), (d)). These results may be explained by its poor sweep volume. Although the injection of CaAlg-8 mM SDS and CaAlg-12 mM SDS fluid can reduce IFT, the effect of displacement efficiency is poor in narrow spaces. The remaining oil in the bound state cannot be effectively swept, resulting in unsatisfactory EOR performance. Capillary force, adsorption force and other factors exist around the bound remaining oil in the tiny pores in the reservoir. Although CaAlg-8 mM SDS and CaAlg-12 mM SDS fluids have a large number of interfaces, which can help them adsorb on the oil–water interface and reduce the mutually repulsion force of oil and water, they cannot penetrate into these small pores well. Thus, the remaining

oil in the bound state cannot be effectively swept out.

3.5.3. Visual characteristics of fluid distribution in porous media

NMR imaging was also performed to observe the changes in fluid distribution. As shown in Fig. 17, the results deeply verify the profile control mechanism, in which CaAlg-SDS plays a significant role in terms of the fluid diversion in heterogeneous reservoirs. The transition from green to yellow to red color in the imaging represents the hydrogen-containing signal from weak to strong, which means that the amount of hydrogen-containing fluid is from small to large; while blue indicates that hydrogen-containing signal is very weak, which means that there is almost no hydrogen-containing fluid. Moreover, lots of pore throats were saturated with water in cores Nos. 1–4 at water saturated stage; while when cores were saturated with oil, due to lack of hydrogen signal in the simulated oil, there was the image of increased blue shaded area. It is worth noting that the fluid is not simply injected into the core, so the increase in the blue shade can only indicate a weakening of the hydrogen-containing signal, that is, the oil is starting to be displaced. In the case of core No. 1 (Fig. 17(a)), the highly permeable layer was saturated with water, and free-state oil in the pores was displaced at the WF stage; despite this displacement, a significant proportion of oil was confined in the pore spaces, denoted by the enduring blue shades discernible in this image. After MF, some of the former blue areas in the hypotonic channels were replaced by new green or even yellow hues, and the original green and yellow also began to deepen, typically as depicted in Fig. 17(b). This proves that the injected water was diverted to the low permeability zone due to the blockage of microspheres in the injection end of the high permeability zone, while starting bound-state oil in these pores.

Afterward, some microspheres are capable with re-migrating in deep high permeable zone during SWF, accompanying subsequent water will continue to divert its origin flow direction into hypotonic layer rich in remaining oil. CaAlg outperforms other fluids at this stage, as the largest coverage of yellow and green tones within Fig. 17(a) infers a comparatively larger sweep scope in the SWF, which probably derives from the effect of elasticity and higher viscosity, as discussed in Section 3.3 and Section 3.5.1. Regarding the entire oil flooding process, similarly, the displacement front presented in Fig. 17(c) does not exhibit a linear pattern. Upon injection of the CaAlg-8 mM SDS microspheres into core No. 3, a plug is first formed in the bottom region of the porous medium, followed by gradual upward proliferation of the yellow and green shades. Notably, among all the cores, core No. 4 exhibits the most conspicuous residual oil saturation (Fig. 17(d)). Although CaAlg-12 mM SDS fluid may lower IFT most appreciably, thereby augmenting the capillary number and enhancing oil washing efficacy, excessive SDS modification can decrease solution viscosity, consequently diminishing the mobility ratio. Coupled with the weakening of viscoelasticity can also decline in sweep efficiency. These results are consistent with those of previous studies.

4. Conclusions

In this thesis, we proposed a novel calcium alginate microsphere microfluidic modulated flooding technology pioneeringly, which can achieve EOR. Various mechanisms involved in profile control and displacement processes were comprehensively characterized and analyzed, including multi-phase interface properties and rheological behavior. The results show that the prepared CaAlg microspheres have good rheological properties including viscosity, viscoelastic, and creep deformation properties, compared with the traditional profile control and flooding agents. By introducing non-polar long carbon chains through compound SDS, the ability to regulate the interphase properties is further strengthened. The mechanism of EOR by microfluidic is the synergistic effect of plugging capacity and displacement of oil. It can be referred that the combination effects of wettability and IFT are the dominant

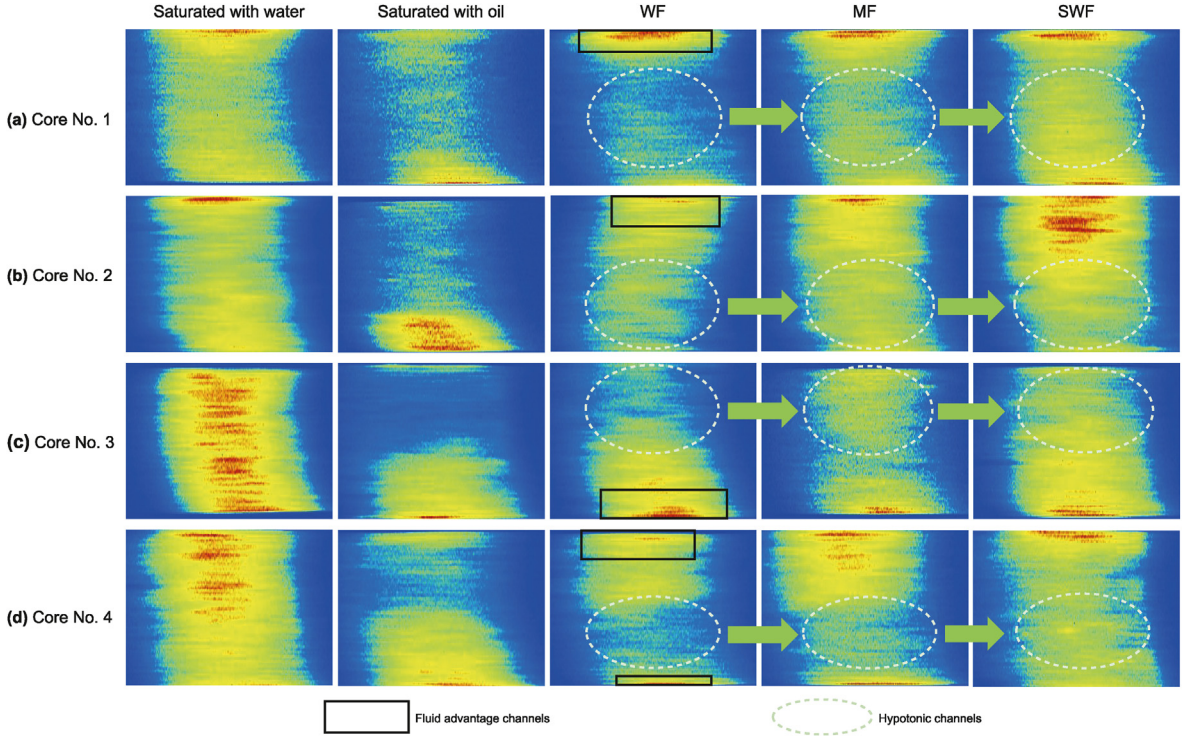

Fig. 17. Nuclear magnetic resonance images of CaAlg (**a**), CaAlg-4 mM SDS (**b**), CaAlg-8 mM SDS (**c**), and CaAlg-12 mM SDS (**d**) with concentration of 2000 mg/L injected into cores Nos. 1–4.

factors of microscope displacement efficiency, and rheological behavior (containing viscoelastic properties) becomes the principal factor of macroscope displacement. From the above results of core flooding and NMR experiments, CaAlg-4 mM SDS fluid exhibits better migration properties, plugging ability and oil recovery potential, which mainly caused by the well-balanced rheological behavior and three-phase interfacial property including IFT and wettability.

The experiment proved that the EOR ability of a series of CaAlg-SDS microspheres with synergistic effect synthesized in this paper is not inferior to that of other previously reported agents. Therefore, we believe that the low-cost, environmentally friendly and biodegradable biomass microsphere system is expected to provide new insights and bring new changes to tertiary recovery. It is expected to be widely used in the process of oilfield exploitation.

CRediT authorship contribution statement

Xiao-Han Zhang: Writing – original draft, Project administration, Investigation, Formal analysis, Data curation. **Chang-Jing Zhou:** Data curation, Conceptualization. **Yuan-Xiang Xiao:** Methodology, Formal analysis, Conceptualization. **Bo Hui:** Supervision. **Yong-Gang Xie:** Supervision. **Yu-Bin Su:** Supervision. **Xin-Ru Li:** Supervision. **Jie Huang:** Validation. **Mao-Chang Liu:** Resources, Project administration, Methodology, Investigation, Funding acquisition, Formal analysis, Data curation, Conceptualization.

Declaration of competing interest

We have consulted the Guide for Authors in preparing our manuscript. We have no known competing financial interests or personal relationships that could have appeared to influence the work reported in this paper. No conflict of interest exits in the submission of this manuscript, and manuscript was approved by all authors for publication.

Acknowledgements

This work was supported by the Open Fund of Shaanxi Key Laboratory of Advanced Stimulation Technology for Oil & Gas Reservoirs (No. KFJJ-TZ-2020-2), the National Natural Science Foundation of China (No. 52104030), the Key Research and Development Program of Shaanxi (No. 2022 KW-35), and the China Fundamental Research Funds for the Central Universities.

References

Bilici, Z., Ozay, Y., Ozbey Unal, B., 2021. Investigation of the usage potential of calcium alginate beads functionalized with sodium dodecyl sulfate for wastewater treatment contaminated with waste motor oil. Water Environ. Res. 93 (11), 2623–2636. https://doi.org/10.1002/wer.1613.

Boul, P.J., Ajayan, P.M., 2020. Nanotechnology research and development in upstream oil and gas. Energy Technol. 8, 1901216. https://doi.org/10.1002/ente.201901216.

Bu, H.T., Kjoniksen, A.L., Knudsen, K.D., Nystrom, B., 2005. Effects of surfactant and temperature on rheological and structural properties of semidilute aqueous solutions of unmodified and hydrophobically modified alginate. Langmuir 21 (24), 10923–10930. https://doi.org/10.1021/la051187g.

Bu, H.T., Kjoniksen, A.L., Elgsaeter, A., Nystrom, B., 2006. Interaction of unmodified and hydrophobically modified alginate with sodium dodecyl sulfate in dilute aqueous solution - calorimetric, rheological, and turbidity studies. Colloids Surf. A Physicochem. Eng. Asp. 278, 166–174. https://doi.org/10.1016/j.colsurfa.2005.12.016.

Cui, S., Cui, C., Ge, S., 2022. The impact of cellulose nanocrystals on the rheology of sodium carboxymethyl cellulose and sodium alginate. J. Appl. Polym. Sci. 139 (38). https://doi.org/10.1002/app.52919.

Dai, C., Liu, Y., Zou, C., 2017. Investigation on matching relationship between dispersed particle gel (DPG) and reservoir pore-throats for in-depth profile control. Fuel 207, 109–120. https://doi.org/10.1016/j.fuel.2017.06.076.

Di, Q.F., Zhang, J.N., Hua, S., 2017. Visualization experiments on polymer-weak gel profile control and displacement by NMR technique. Petrol. Explor. Dev. 44 (2), 294–298. https://doi.org/10.1016/s1876-3804(17)30033-2.

Ding, M.S., Wang, J., Lin, J.Z., 2017. Potential application of biosurfactants mixtures in high-temperature and high-salinity reservoirs. Petrol. Sci. Technol. 35 (12), 1189–1195. https://doi.org/10.1080/10916466.2016.1225088.

Garcia, A.R., Lacko, C., Snyder, C., 2017. Processing-size correlations in the preparation of magnetic alginate microspheres through emulsification and ionic crosslinking. Colloids Surf. A Physicochem. Eng. Asp. 529, 119–127. https://doi.org/10.1016/j.colsurfa.2017.05.058.

Gbadamosi, A.O., Junin, R., Manan, M.A., 2018. Recent advances and prospects in polymeric nanofluids application for enhanced oil recovery. J. Ind. Eng. Chem. 66, 1–19. https://doi.org/10.1016/j.jiec.2018.05.020.

Ghandi, E., Parsaei, R., Riazi, M., 2019. Enhancing the spontaneous imbibition rate of water in oil-wet dolomite rocks through boosting a wettability alteration process using carbonated smart brines. Petrol. Sci. 16 (6), 1361–1373. https://doi.org/10.1007/s12182-019-0355-1.

Hecht, H., Srebnik, S., 2016. Structural characterization of sodium alginate and calcium alginate. Biomacromolecules 17 (6), 2160–2167. https://doi.org/10.1021/acs.biomac.6b00378.

Hu, W.R., Wei, Y., Bao, J.W., 2018. Development of the theory and technology for low permeability reservoirs in China. Petrol. Explor. Dev. 45 (4), 685–697. https://doi.org/10.1016/s1876-3804(18)30072-7.

Jay, S.M., Saltzman, W.M., 2009. Controlled delivery of VEGF via modulation of alginate microparticle ionic crosslinking. J. Contr. Release 134 (1), 26–34. https://doi.org/10.1016/j.jconrel.2008.10.019.

Li, Y., Dai, C., Zhou, H., 2018. Investigation of spontaneous imbibition by using a surfactant-free active silica water-based nanofluid for enhanced oil recovery. Energy & Fuels. 32 (1), 287–293. https://doi.org/10.1021/acs.energyfuels.7b03132.

Li, Z., Kang, W.-L., Li, M.-L., 2023. Surface-functionalized cellulose nanocrystals (CNC) and synergisms with surfactant for enhanced oil recovery in low-permeability reservoirs. Petrol. Sci. 20 (3), 1572–1583. https://doi.org/10.1016/j.petsci.2022.11.010.

Li, Z.K., Li, D.C., Hao, D., 2017. Study on the creep and recovery behaviors of ferrofluids. Smart Mater. Struct. 26 (10). https://doi.org/10.1088/1361-665X/aa8835.

Liu, T., Gou, S., Zhou, L., 2021. High-viscoelastic graft modified chitosan hydrophobic association polymer for enhanced oil recovery. J. Appl. Polym. Sci. 138 (11). https://doi.org/10.1002/app.50004.

Liu, X., Wen, Y., Qu, J., 2019. Improving salt tolerance and thermal stability of cellulose nanofibrils by grafting modification. Carbohydr. Polym. 211, 257–265. https://doi.org/10.1016/j.carbpol.2019.02.009.

Masulli, M., Liu, Z.-L., Guo, F.-Z., 2022. Temperature effect on the dynamic adsorption of anionic surfactants and alkalis to silica surfaces. Petrol. Sci. 19 (4), 1866–1876. https://doi.org/10.1016/j.petsci.2021.11.008.

Muggeridge, A., Cockin, A., Webb, K., 2014. Recovery rates, enhanced oil recovery and technological limits. Phil. Trans. Math. Phys. Eng. Sci. 2006, 372. https://doi.org/10.1098/rsta.2012.0320.

Parekh, P., Parmar, A., Chavda, S., 2011. Modified calcium alginate beads with sodium dodecyl sulfate and clay as adsorbent for removal of methylene blue. J. Dispersion Sci. Technol. 32 (10), 1377–1387. https://doi.org/10.1080/01932691.2010.505113.

Pu, W., Shen, C., Wei, B., 2018a. A comprehensive review of polysaccharide biopolymers for enhanced oil recovery (EOR) from flask to field. J. Ind. Eng. Chem. 61, 1–11. https://doi.org/10.1016/j.jiec.2017.12.034.

Pu, W., Zhao, S., Wang, S., 2018b. Investigation into the migration of polymer microspheres (PMs) in porous media: implications for profile control and oil displacement. Colloids Surf. A Physicochem. Eng. Asp. 540. https://doi.org/10.1016/j.colsurfa.2018.01.018.

Shariatpanahi, S.F., Hopkins, P., Aksulu, H., 2016. Water based EOR by wettability alteration in dolomite. Energy & Fuels. 30 (1), 180–187. https://doi.org/10.1021/acs.energyfuels.5b02239.

Smith, J.E., 1989. The transition pressure: a quick method for quantifying polyacrylamide gel strength. SPE International Symposium on Oilfield Chemistry. https://doi.org/10.2118/18739-MS.

Wang, B., Lin, M.Q., Guo, J.R., 2016. Plugging properties and profile control effects of crosslinked polyacrylamide microspheres. J. Appl. Polym. Sci. 133 (30). https://doi.org/10.1002/app.43666.

Wang, K., You, Q., Long, Q.-M., 2023. Experimental study of the mechanism of nanofluid in enhancing the oil recovery in low permeability reservoirs using microfluidics. Petrol. Sci. 20 (1), 382–395. https://doi.org/10.1016/j.petsci.2022.09.026.

Wang, S., Tang, Z., Qu, J., 2021. Research on the mechanisms of polyacrylamide nanospheres with different size distributions in enhanced oil recovery. RSC Adv. 11 (10), 5763–5772. https://doi.org/10.1039/d0ra09348c.

Wang, Z.-Y., Lin, M.-Q., Li, H.-K., et al., 2022. Plugging property and displacement characters of a novel high-temperature resistant polymer nanoparticle. Petrol. Sci. 19 (1), 387–396. https://doi.org/10.1016/j.petsci.2021.08.010.

Yakasai, F., Jaafar, M.Z., Bandyopadhyay, S., 2021. Current developments and future outlook in nano fluid flooding: a comprehensive review of various parameters in fluencing oil recovery mechanisms. J. Ind. Eng. Chem. 93, 138–162. https://doi.org/10.1016/j.jiec.2020.10.017.

Zhang, M.J., Hong, H.C., Lin, H.J., 2018. Mechanistic insights into alginate fouling caused by calcium ions based on terahertz time-domain spectra analyses and DFT calculations. Water Res. 129, 337–346. https://doi.org/10.1016/j.watres.2017.11.034.

Zhang, X., Deng, J.-N., Yang, K., 2022. High-strength and self-degradable sodium

alginate/polyacrylamide preformed particle gels for conformance control to enhance oil recovery. Petrol. Sci. 19 (6), 3149–3158. https://doi.org/10.1016/j.petsci.2022.06.012.

Zhao, Y., Zhuang, J., Wang, Y., 2020. Improvement of loess characteristics using sodium alginate. Bull. Eng. Geol. Environ. 79 (4), 1879–1891. https://doi.org/10.1007/s10064-019-01675-z.

Zhou, Y., Wu, X., Zhong, X., 2019. Surfactant-augmented functional silica nanoparticle based nanofluid for enhanced oil recovery at high temperature and salinity. ACS Appl. Mater. Interfaces 11 (49), 45763–45775. https://doi.org/10.1021/acsami.9b16960.

Zou, J., Yue, X., Dong, J., 2020. Novel in-depth profile control agent based on in-situ polymeric microspheres in low permeability reservoir. J. Dispersion Sci. Technol. 41 (8), 1254–1264. https://doi.org/10.1080/01932691.2019.1699423.